A modified multi-objective sorting particle swarm optimization and its application to the design of the nose shape of a high-speed train

Shuanbao Yao, Dilong Guo, Zhenxu Sun & Guowei Yang

Taylor & Francis
Taylor & Francis Group

A modified multi-objective sorting particle swarm optimization and its application to the design of the nose shape of a high-speed train

Shuanbao Yao[a], Dilong Guo[b], Zhenxu Sun[b]* and Guowei Yang[b]

[a]National Engineering Research Center for High-speed EMU, CSR Qingdao Sifang Locomotive Co., Ltd., Qingdao, China; [b]Key Laboratory for Mechanics in Fluid Solid Coupling Systems Institute of Mechanics, Chinese Academy of Sciences, Beijing, China

Based on the concepts of niche count and crowding distance, a modified multi-objective particle swarm optimization (MPSO) is introduced. The niche count and crowding distance are used to determine the globally best particle across four test cases using an external file. A comparative analysis was carried out between MPSO and non-dominated sorting multi-objective adaptive genetic algorithms, both real-coded and binary-coded. The results show that MPSO based on the crowding distance is best for getting the Pareto front, especially for problems with high-dimensional and non-continuous Pareto fronts. In order to verify the efficiency of MPSO in solving engineering problems, the optimal design of the aerodynamic nose shape of high-speed trains was undertaken using a modified vehicle modeling function (MVMF) parametric method. Taking the aerodynamic drag of the whole train (Cd) and the aerodynamic lift of the trailer car (Cl) as the optimization goals, the Kriging surrogate model was introduced to reduce the computational time, and the MPSO based on crowding distance was used to find the Pareto front. The optimization results show that MPSO is efficient at getting the Pareto front; compared to the original shape, the Cd and Cl of the optimal shape are reduced by 1.6% and 29.74%, respectively.

Keywords: multi-objective particle swarm optimization; crowding distance; VMF parameterization; aerodynamic shape; high-speed trains

1. Introduction

The multi-objective optimization problem is very common in many areas of engineering design, and it becomes difficult to meet the needs of practical problems using the traditional gradient algorithm as the complexity of the problems increases. In order to overcome the disadvantage of gradient algorithms that are highly sensitive to the initial values and difficult to use to obtain global optimization, scholars have proposed many global optimization algorithms based on population search (Deb, Mohan, & Mishra, 2005; Fonseca & Fleming, 1994; Pratab & Deb, 2000; Srinivas & Dep, 1994). Inspired by the foraging behavior of a flock of birds, Kennedy and Eberhart (1995) proposed particle swarm optimization (PSO), which is simple and easy to implement and has been developing rapidly in recent years. Moore and Chapman (1999) used PSO to solve the multi-objective optimization problem for the first time; since then, there have been many different versions of the multi-objective particle swarm optimization algorithm (Coello, Pulido, & Lechuga, 2004; Hu & Eberhart, 2002; Li, 2003; Parsopoulos & Vrahatis, 2002). Coello et al. (2004) used an external file to save every flight experience of particles, divide the search space into a hypercube, the fitness of which is determined by the number of particles it contains, choose one hypercube through the roulette

method based on hypercube fitness, and then select a particle from the hypercube randomly to be the global best particle. Li (2003) proposed an Non-dominated Sorting Particle Swarm Optimization (NSPSO) based on the idea of non-dominated sorting, and the niche count and crowding distance are introduced into NSPSO. Test results show that the performance of NSPSO is better than that of Non-dominated Sorting Genetic Algorithm II (NSGA-II) (Deb et al., 2005).

Based on the findings of the above literature, this paper proposes a modified PSO for which the global best particle is determined by feeding the niche count and crowding distance into an external file. The niche count and crowding distance are both used to describe the particle distribution, and in most cases different particles have the same niche count. Therefore, we use three methods to select the global best particles in an external file. The first method computes the niche count of every particle and is named the modified PSO with niche count (MPSO-NI). The second approach computes the crowding distance of every particle and is named the modified PSO with crowding distance (MPSO-CR). The third method computes the niche count and crowding distance of every particle simultaneously, but taking the niche count as the first criteria, and is named the modified PSO with niche count and crowding distance

---

*Corresponding author. Email: sunzhenxu@imech.ac.cn

(MPSO-NC). With the comparison of test functions, it was found that the crowding distance can guide particles to the optimal solution more efficiently, that MPSO-CR performs better than the other two algorithms, and that MPSO-NC performs better than MPSO-NI. Compared to the adaptive binary-range genetic algorithms (ABGAs) and the adaptive real-range genetic algorithms (ARGAs; Arakawa & Hagiwara, 1998; Yang, Chen, & Cui, 2009), MPSO performs better in terms of obtaining the Pareto front.

In order to verify the efficiency of MPSO in engineering problems, the multi-objective optimization design of the aerodynamic nose shape of high-speed trains (Ku et al., 2010) is performed using MPSO-CR. The aerodynamic drag of the whole train (with a leading car, a middle car and a trailing car included) and the aerodynamic lift of the trailing car are treated as the optimization objectives so as to improve the operational safety and energy-saving ability of trains. The Kriging surrogate model is used in place of the numerical simulation in order to reduce the computation time. A modified vehicle modeling function parametric approach is proposed to describe the complex three-dimensional geometry (Ku et al., 2010; Rho et al., 2009). The optimization results show that MPSO-CR can be applied to the task of solving complex engineering problems. The optimization processes proposed in this paper can shorten the design cycle of the aerodynamic shape of high-speed trains, improve design efficiency and provide a reference for the multi-objective optimization design of the aerodynamic shape of high-speed trains.

2. Modified multi-objective non-dominated sorting particle swarm optimization

As to the basic PSO, the personal best particle *pbest* and the global best particle *gbest* are used to update the position and flight speed of each particle, and guide other particles to move to *pbest* and *gbest*. The position vector of a single particle takes the form of $X_i = (x_{i,1}, x_{i,2}, \ldots, x_{i,d})$, and its flight speed is $V_i = (v_{i,1}, v_{i,2}, \ldots, v_{i,d})$. The formulas of particle position and velocity updating are as follows:

$$v_{i,j}(t+1) = wv_{i,j}(t) + c_1 r_1 (p\text{best}_{i,j} - x_{i,j}(t)) + c_2 r_2 (g\text{best}_j - x_{i,j}(t))$$
$$x_{i,j}(t+1) = x_{i,j}(t) + v_{i,j}(t+1) \quad (1)$$

where, $i = 1, 2, \ldots, N, j = 1, 2, \ldots, D, N$ is the size of the particle population, D is the component size of the particle position vector (the dimension size of the design space), w is the inertia weight, c_1 and c_2 are two coefficients, and r_1 and r_2 are two random numbers within the range [0,1]. In order to prevent particles from flying too fast and affecting the convergence of the algorithm, a maximum flight speed $v_{\max}$ is usually given. If $v_{i,j}(t+1)$ is greater than $v_{\max}$, the value of $v_{i,j}(t+1)$ should be resized as $v_{\max}$. PSO has been applied in many fields for single objective optimization,

and has achieved many perfect results (Dehuri, Roy, Cho, & Ghosh, 2012).

When comparing multi-objective PSO with single-objective PSO, the obvious difference is how to determine *gbest*. The solution for the multi-objective optimization problem is a Pareto front set in which none of the particles are better than others. Thus, the key factor in determining the performance of multi-objective PSO is how to select *gbest* from the Pareto front. The particle *gbest* should be able to ensure the diversity of the population so as to adequately guide other particles moving to the Pareto front in the design space. So *gbest* should be a particle in the Pareto front of every iteration and be at the sparse area of the design space.

As the number of objectives increases, the number of non-dominated solutions increases dramatically, which reduces the selection pressure inside the population. It is difficult to determine the suitable *gbest* if the multi-objective PSO only takes the non-dominated relationship among Pareto solutions as the criterion, which may have a bad effect on the optimization trajectory of particles and the diversity of the population, and then deteriorate the convergence of the algorithm. In order to keep appropriate selection pressure and the diversity of population, *gbest* and *pbest* are determined according to an external file, the niche count and the crowding distance of the Pareto front in this paper.

2.1. Niche count

The niche count is firstly introduced by genetic algorithms, the main idea of which is as follows. The population of each generation is divided into several categories, then a number of outstanding individuals are selected to compose a new population according to the fitness of each individual. After this, the original population is updated through genetic manipulation among the new populations. The niche count can maintain the diversity of the population and may improve the global optimization capability and the convergence rate of genetic algorithms. The key variable of the niche count is the niche radius. The niche count with sharing mechanism is usually used in genetic algorithms and the niche radius should be determined manually, which is hard to achieve. Based on the position variation of the particles in the iterative process, the following formula to determine the niche radius can be obtained:

$$\sigma_s = \frac{\sum_{i=1}^{m}(u_i - l_i)}{n-1};$$

where u_i is the maximum value of the objective function of the population, l_i is the minimum value of the objective function and n is the number of particles. As shown in Figure 1, the *nicount* of a particle is calculated within a circle with the position of this particle as its center and the niche radius as its radius. The distance between adjacent
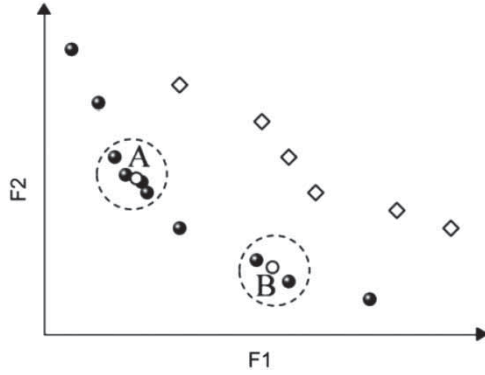
Figure 1.   Schematic drawing for niche count.

Figure 2.   Schematic drawing for crowding distance.

particles is obtained by the Euclidean distance. It can be seen that *nicount* can be the same for different particles on some occasions, which decreases the judgment ability. The greater the *nicount* value, the shorter the distance between the particles and the less diversity of the population. As a result, the optimal value of *nicount* should be the minimum value of all particles in the population.

2.2.   Crowding distance

The crowding distance (Pratab & Deb, 2000) is used to calculate the distance between a particle in a non-dominated front solution set with the other particles of the front so as to characterize the degree of congestion between particles. Obviously, the greater the value of congestion distance, the lower the degree of congestion between the particles and thus the better the diversity of the population.

As shown in Figure 2, the crowding distance of particle *i* can be calculated by

$$I_{\text{dis}} = \sum_{k=1}^{m} (f_k(i-1) - f_k(i+1)),$$

and as shown above, the greater I_{dis} is, the greater the distance between particles is and the better the diversity of the population which can be obtained. In NSGA-II, the crowding distance of the particles which are on the non-dominated boundary is set to infinity to ensure that these particle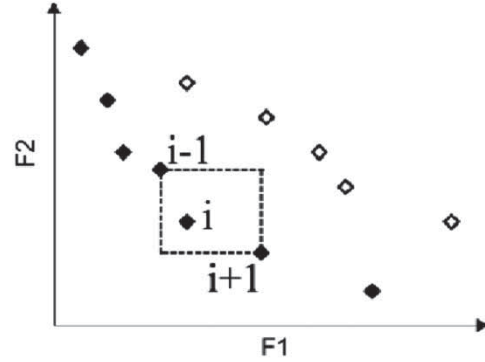s could not be eliminated. However, in MPSO, if the above strategy is still utilized, *gbest* would always be a particle in the initial non-dominated front. As a result, the crowding distance will no longer determine *gbest*. With the use of external files, the boundary particles in the initial non-dominated front will be preserved in the external file automatically, which will not be eliminated due to the short crowding distance. Meanwhile, little influence on the calculated Pareto optimal set could be exerted by other non-dominated front sets. As a result, a relatively small value is given to each non-dominated boundary particle in this paper.

2.3.   External files

An external file (Coello et al., 2004) is used to store the Pareto front during the searching process. All the particles in the external file should be non-dominated with each other, therefore the particles in the external file need to be re-sorted according to the non-dominated rank after each iteration, so that only the particles in the first non-dominated rank are saved in the external file. Then, *gbest* is determined according to the niche count and crowding distance of the Pareto front in the external file. After the introduction of an external file, the number of particles in the Pareto front is free from the size of the initial particle population, which may obtain more Pareto-optimal solutions.

Figure 3 shows the basic MPSO flow. First, the particle population is initialized to get the position and velocity
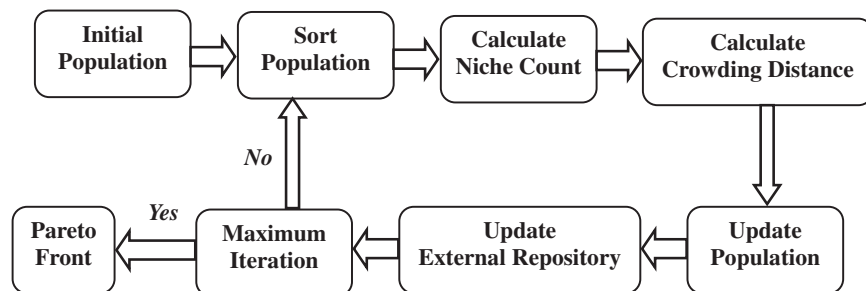

Figure 3.   MPSO algorithm flowchart.

of the particles in the initial population, and the particle position is set as the initial value of *pbest*. Next, the non-dominated rank of the population is sorted according to the fitness of the particle. Then the niche count and crowding distance of each particle are calculated. Based on *nicount* and I_{dis}, *gbest* and the external file are initialized. Based on *pbest* and *gbest*, the population is updated and the descendant population is obtained. Then a reorder of the descendant population is performed and the Pareto front is added to the external file. The particles in the external files are also sorted, with the Pareto front preserved while others are deleted, and *gbest* is obtained according to *nicount* and I_{dis}. If iteration steps reach the maximum, the Pareto optimal solution set in the external file will be outputted, otherwise the algorithm will step into the next iteration.

3. Experiments

3.1. Test functions

In order to verify the efficiency of the optimization algorithm, four test functions (all functions are minimized; see Li, 2003; Pratab & Deb, 2000) are used to test the algorithms introduced in this paper:

$$\text{TEST1}: \begin{cases} f_1(x) = x_1 \\ f_2(x) = g(x)h(x); \end{cases}$$

$$0 \leq x_1 \leq 1, -30 \leq x_2 \leq 30;$$

$$g(x) = 11 + x_2^2 - 10\cos(2\pi x_2);$$

$$h(x) \begin{cases} 1 - \sqrt{\dfrac{f_1(x)}{g(x)}} & f_1(x) \leq g(x). \\ 0, & \text{otherwise} \end{cases}$$

$$\text{TEST2}: \begin{cases} f_1(x) = x_1 \\ f_2(x) = (1 + 10x_2) \\ \left[1 - \left(\dfrac{x_1}{1 + 10x_2}\right)^2 - \dfrac{x_1}{1 + 10x_2}\sin(8\pi x_1) \right]; \end{cases}$$

$$0 \leq x_1, x_2 \leq 1.$$

$$\text{TEST3}: \begin{cases} f_1(x) = \sum_{i=1}^{2}\left[-10\exp\left(-0.2\sqrt{x_i^2 + x_{i+1}^2}\right) \right] \\ f_2(x) = \sum_{i=1}^{3}(|x_i|^{0.8} + 5\sin(x_i^3)); \end{cases}$$

$$-5 \leq x_i \leq 5, i = 1, 2, 3.$$

$$\text{TEST4}: \begin{cases} f_1(x) = 1 - \exp(-4x_1)\sin^6(6\pi x_1) \\ f_2(x) = g(x)(1 - (f_1(x)/g(x))^2); \end{cases}$$

$$0 \leq x_i \leq 1, i = 1, 2, \ldots, 10;$$

$$g(x) = 1 + 9\left(\sum_{i=2}^{10}\dfrac{x_i}{9}\right)^{0.25}.$$

The Pareto optimal solution sets of the four test functions are discontinuous solution sets, of which TEST4 owns 10 dimensions, which could be effectively used to test the optimization capability for the algorithms in solving multimodal, discontinuous and high-dimensional problems. For all test functions, the initial particle population is 200 and the number of iterations is 1000. To improve the search capability of the algorithm during the iterative process, w is gradually reduced from 1.2 to 0.4 during the iteration, while c_1 and c_2 are 2, and the maximum speed v_{max} is half the difference between the maximum value and the minimum value for each dimension in the design space.

Table 1. Test results from the different algorithms.

	TEST1			**TEST2**		
	SP	D	Number	SP	D	Number
MPSO-NC	0.03225	1.13551	57.1	0.02038	1.68997	367.2
MPSO-NI	0.75410	1.02361	34.1	0.02229	**1.69031**	325.5
MPSO-CR	**0.01482**	**1.25632**	**142.6**	**0.01617**	1.69026	**560.3**
ABGA	34.34229	N/A	120.3	0.26940	N/A	198.4
ARGA	38.54076	N/A	59.1	0.19126	N/A	122.3

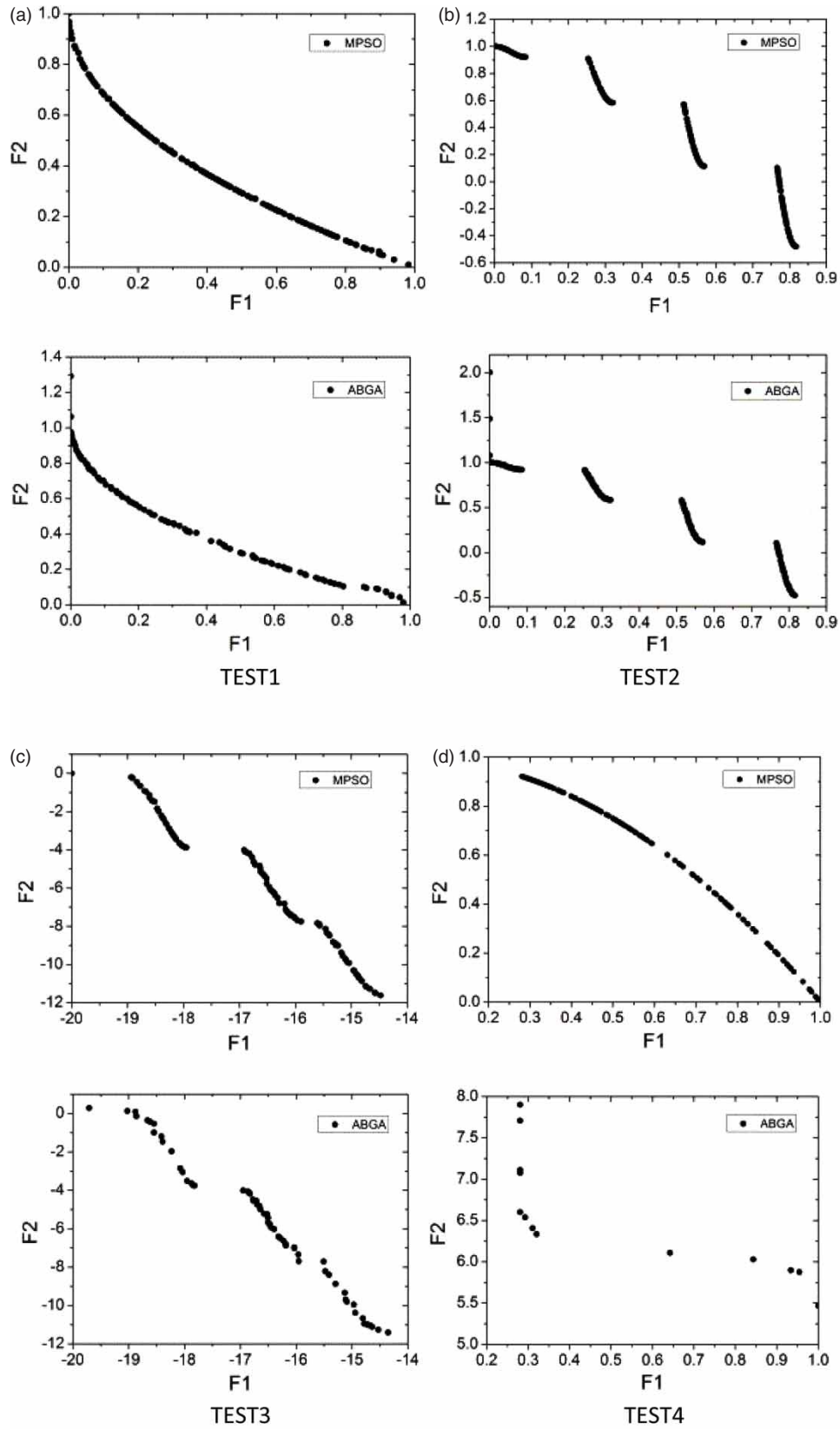|	**TEST3**			**TEST4**		
	SP	D	Number	SP	D	Number
MPSO-NC	0.16186	12.67251	**130.1**	0.02422	1.16868	227.1
MPSO-NI	0.29671	12.51064	75.2	0.01394	1.16855	233.2
MPSO-CR	0.19456	12.50832	126.8	**0.00995**	**1.16868**	**496.0**
ABGA	0.24482	12.82375	60	N/A	N/A	N/A
ARGA	**0.15978**	**12.84945**	111.8	N/A	N/A	N/A

Figure 4.   Pareto-optimal solution sets obtained by MPSO-CR and the ABGA.

3.2. Performance metrics of the Pareto front

In order to effectively analyze the quality of the non-dominated solutions obtained from all algorithms, the spacing metrics (Schott, 1995) and maximum spreading range assessment are used to compare the optimal solution sets of the test functions.

Spacing metrics can evaluate the distribution of non-dominated solution set uniform or not, which is calculated as

$$SP = \sqrt{\frac{1}{n-1}\sum_{i=1}^{n}(\bar{d}-d_i)^2},$$

in which, $d_i = \min_j \left(\sum_{k=1}^{m}|f_m^i - f_m^j|\right); i,j = 1,2,\ldots,$ n, $i \neq j$, n is the amount of Pareto optimal solutions, m

is the amount of optimization objectives, and $\bar{d}$ is the mean value of all d_i. When SP is zero, it means that all non-dominated solutions are equally distributed. Thus, the smaller SP is, the better the uniformity of the distribution of the solution set.

The maximum spreading range assessment can effectively test the scope of extremal solutions in the objective function space, calculated as

$$D = \sqrt{\sum_{k=1}^{m}(\max_{i=1}^{n}f_i^k - \min_{i=1}^{n}f_i^k)}$$

in which n is the amount of Pareto optimal solutions and m is the amount of optimization objectives. It is apparent from the definition that the larger the value of D, the closer
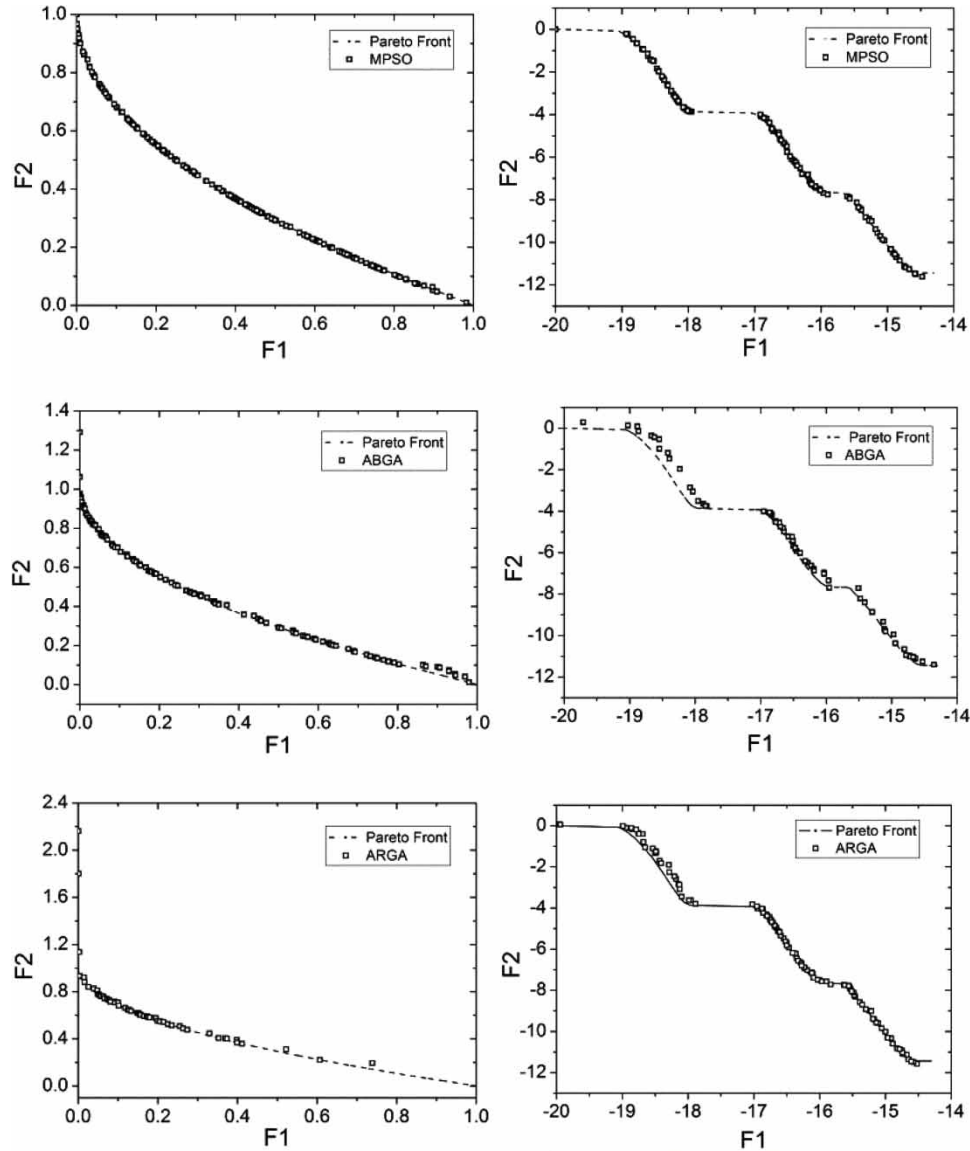

Figure 5. Comparison of the real Pareto solutions and the numerical results obtained from MPSO-CR, the ARGA and the ABGA (TEST1 and TEST3).

the extremum of the Pareto optimal solution set is to real extremum; further, the larger the distribution range of the solution set is, the better it performs.

3.3. Results of the test functions

ABGAs and ARGAs are both based on the idea of non-dominated sorting and the niche count concept. The difference between the two types is just the coding method, which has a strong effect on search performance. Details of the two methods can be found in Yang et al. (2009), Arakawa and Hagiwara (1998), and Yao, Guo, Sun, Yang, and Chen (2012). For each test function, each algorithm runs 10 times independently. Table 1 shows the average of 10 results of every algorithm. As can be seen, MPSO-CR performs significantly better than the other algorithms for TEST1 and TEST4, and obtains more Pareto-optimal solutions and better distribution uniformity than other algorithms for TEST2, but has a worse maximum dispersion scope of the solution set than MPSO-NI; 10 times optimization results of the ABGA and ARGA do not fully converge to the Pareto-optimal solution set nearby for TEST1, TEST2 and TEST4. For TEST1 and TEST2, both algorithms do not converge to the Pareto-optimal solution set just in the boundary points, but do not converge to the Pareto-optimal solution set at all for TEST4. This means that the searching capability of these two kinds of algorithms for high-dimensional problems is weak. For TEST3, the distribution uniformity and the maximum dispersion scope of the optimal solution set obtained by the ARGA are superior to other algorithms, but the amount of solutions is less than for MPSO-NC and MPSO-CR. Considering the test results of the four test functions, MPSO-CR has the best optimization capability; in addition, the number and performance of the result are better. In contrast, the performance of the ABGA is the worst.

In order to directly understand the distribution of Pareto-optimal solutions obtained by each algorithm, Figure 4 shows the best Pareto-optimal solution of these four test functions obtained by MPSO-CR and by the ABGA. As can be seen, after 1000 iterations, the upper boundary points of the Pareto-optimal solutions obtained by the ABGA for TEST1 and TEST2 do not converge with the optimal solution, and its distribution is worse than MPSO-CR. For TEST3, the ABGA has a bigger first objective value F1 than MPSO-CR but a smaller second objective value F2, and the difference is greater. Furthermore, the maximum spreading range D of ABGA, which is decided by F1 and F2, is bigger than that of MPSO-CR. This means that D can effectively test the range of the extreme points in the objective function space. For TEST4, ABGA obtains several local extreme points and does not find the Pareto-optimal solution.

In Figure 5, the distribution of the Pareto-optimal solutions obtained by MPSO-CR, the ARGA and the ABGA

for TEST1 and TEST3 is given near the real Pareto-optimal solutions. It can be seen that MPSO-CR has the best distribution. For TEST1, the convergence, distribution uniformity and maximum dispersion range of the Pareto-optimal solutions obtained by MPSO-CR are superior to those obtained by the ARGA and the ABGA. The ARGA has a better result in searching the first objective value F1 than in searching the second objective value F2, which leads to a worse distribution of the lower part of the Pareto front solution set. It also can be seen that the convergence of MPSO-CR is obviously superior to the ABGA.

4. Optimal aerodynamic shape design of high-speed trains

As the running speed of high-speed trains increases, the aerodynamic problems are increasingly prominent, and thus good aerodynamic performance is a key issue for the nose shape of high-speed trains. In order to obtain a streamlined design with excellent aerodynamic performance and improve the optimization efficiency of a train head's aerodynamic shape, many scholars have done a lot of work (Kwon et al., 2001; Lee & Kim, 2008; Sun, Song, & An, 2010; Vytla, Huang, & Penmetsa, 2010; Yao, Guo, et al., 2012; Yao, Guo, & Yang, 2012). Lee and Kim (2008) developed an optimization algorithm that combines successive quadratic programming (SQP) optimization with a support vector machine in order to reduce micro-pressure. Yao, Guo, et al. (2012) introduced genetic algorithms to reduce the aerodynamic drag of high-speed trains and the lift force of the trailing car. Taking the aerodynamic drag and noise as optimal objectives, Vytla et al. (2010) used a hybrid genetic-PSO algorithm to optimize a two-dimensional nose shape. There are usually many design variables for engineering the nose shape of high-speed trains, and it is very difficult to find the Pareto-optimal solutions if the multi-objective optimization method is not good enough. In section 3, the test function results showed that MPSO-CR is superior to MPSO-NI, MPOS-NC, the ABGA and the ARGA. In order to test the engineering application of the optimal method proposed in this paper, we will use MPSO-CR to optimize the three-dimensional nose shape of a high-speed train to reduce both the aerodynamic drag of the whole train and the lift force of trailing car. Because the train runs near to the ground, has a complex operating environment and is affected by ground effect, the flow field results around the train is very complex and requires more CFD computational time and higher accuracy. In order to reduce the computational cost, only the nose shape of the train is considered in this paper; the bogies, windshields, pantograph and other ancillary components are all ignored. The parametric method of the streamline, CFD computing method and the construction of the Kriging surrogate model are detailed in the following sections.

4.1. Three-dimensional parametric method for streamlining the nose shape of a high-speed train

The Free Form Deformation (FFD) and Non-Uniform Rational B-Splines (NURBS) methods are widely used in the field of parameterized geometry. But for the three-dimensional parameterization of a complex surface, their application is problematic due to practical engineering optimization requiring far more design variables. This means that a higher optimization capability is needed for the optimization algorithm, and is not conducive to constructing the response surface model with higher prediction accuracy. For applications of aerodynamic shape engineering optimization problems that require a large amount of computational cost (for example, millions or even tens of millions grids are required to calculate a sample point), both methods are useless. In order to solve this problem, Kulfan and Bussoletti (2006) proposed the class and shape function parametric method and realized the 2D and 3D parametric designs of the airfoil, wing and fuselage. On this basis, Rho et al. (2009) proposed the VMF 3D parametric approach and used less design parameters to realize 3D parametric designs of the complex shape of the automobiles. Ku et al. (2010) applied the VMF method to the 3D parametric design of streamlining high-speed trains. In this paper, in order to better describe the aerodynamic shape of high-speed trains, the VMF method is appropriately corrected and the local shape boundary is described by some simple but effective functions instead.

The streamlined head of high-speed trains is controlled by the critical two-dimensional line, and surface configuration is formed by the gradual changes of the key parameters of the profile equation. According to the basic outline of the currently existing models, basic lines and control points are extracted (see Figure 6). The overall outline of the streamlined head is controlled by four main contour lines and two local contour lines, and the shape of the cab is formed by superimposing separate surface control equations onto the basic surface. According to the basic properties of all the profile equations, nine control points are extracted to determine the boundary of the profile.

With P1 as the origin point of the coordinate, the length direction of the head as the x axis and the width direction of the head as the y axis, a basic coordinate system can be established by the right-hand rule. The parametric equations of each profile are given as follows:

The upper longitudinal section profile equation is

$$Z(x) = \left(\frac{x}{x_{p7}}\right)^{A_{11}} \left(1 - \frac{x}{x_{p7}}\right)^{A_{12}} z_{p7} + \frac{x z_{p7}}{x_{p7}}.$$

The bottom longitudinal section profile equation is

$$Z(x) = \frac{x^{A_{21}}}{z_{p2}}.$$

The horizontal section profile equation is

$$Y(x) = \left(\frac{x}{x_{p8}}\right)^{A_{31}} \left(1 - \frac{x}{x_{p8}}\right)^{A_{32}} y_{p8} + \left(1 - \frac{x}{x_{p8}}\right) y_{p1} + \frac{x y_{p8}}{x_{p8}}.$$

The maximum cross-sectional profile equation is

$$Z(y) = \frac{z_{p7} y^{A_{41}} (2 y_{p8} - y)^{A_{42}}}{(y_{p8}^{A_{41}+A_{42}} g(y))},$$

in which, $g(y) = \min\{(y/y_{p8})^{0.5}, 1\}$.

The minimum cross-section profile is a circle, and its equation is

$$Z(y) = (R^2 - y^2)^{0.5} - R,$$

in which, R is the radius and the equation converges to a point at point P1.
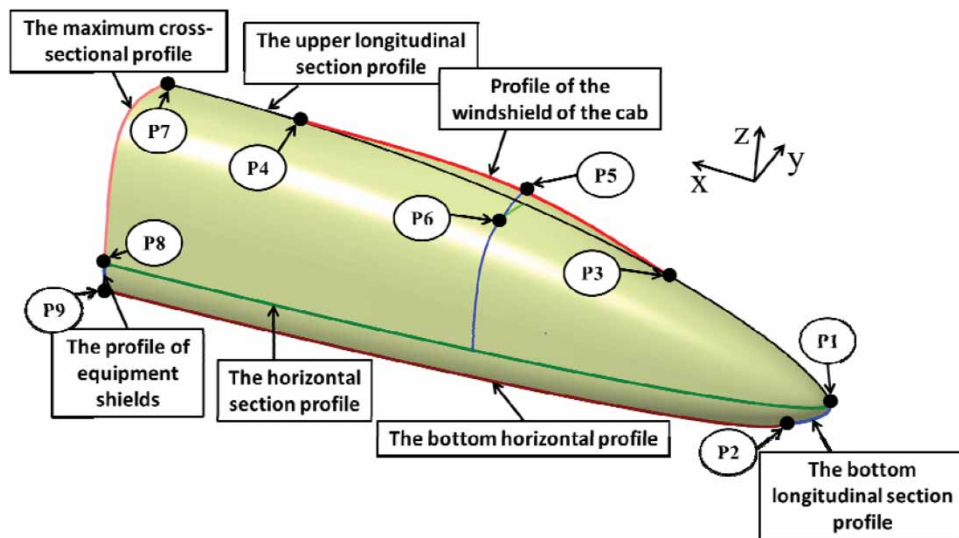

Figure 6.   Basic profile lines and control points in VMF parametric design.

Table 2. Design variables and their ranges.

Design variable	Range	Design variable	range
A_{11}	(0.3,0.6)	P_u	(0.0,2.0)
A_{12}	(2.0,5.0)	g_h	(0.3,0.5)
A_{21}	(0.2,0.5)	A_{61}	(0.6,1.0)

The bottom horizontal profile equation is

$$Y(x) = \left(\frac{x}{x_p}\right)^{A_{51}} \left(1 - \frac{x}{x_p}\right)^{A_{52}} y_{p9} + \left(1 - \frac{x}{x_p}\right) y_{p1} + \frac{x y_{p9}}{x_p},$$

in which $x_p = x_{p9} - x_{p2}$.

The equation for the nose shape surface is

$$Z(y) = z_p \left(1 - \left(\frac{(y - y_p)}{y_p}\right)^{A_m}\right)^{1/A_m},$$

in which, $A_m = A_{R1} + (A_{41} - A_{R1})(x/L)^{P_u}$, L is the length of the streamlined head, y_p is the y coordinate of the horizontal section profile, and z_p is the z coordinate of the upper longitudinal section profile.

The surface equation of the windshield of the cab is

$$Z(x) = g_h \left(\sin\left(\pi\left(\frac{(x - x_{p3})}{(x_{p4} - x_{p3})}\right)^{A_{61}}\right)\right)^{A_{62}}$$
$$\left(\cos\left(\frac{\pi(y - y_{p5})}{(y_{p6} - y_{p5})/2}/2\right)\right)^{A_{63}},$$

in which g_h can control the viewing angle, the x-direction coordinate values of control points P3, P4, P5 and P6 are unchanged, the y- and z-direction coordinate values just change with the variation of the base surface, A_{61} and A_{62} control the x-direction deformation of the windshield, and A_{63} controls the y-direction deformation of the windshield.

The surface equation of the equipment shields is

$$X(z) = \frac{z^2(x_{pb} - x_{pc})}{z_{p2}^2 + x_{pc}},$$

$$Y(z) = \frac{z^2(y_{pb} - y_{ph})}{z_{p2}^2} + y_{ph},$$

in which x_{pb} is the x coordinate of the bottom horizontal profile, x_{pc} is the x coordinate of the upper longitudinal section profile, y_{pb} is the y coordinate of the bottom longitudinal section profile, and y_{ph} is the y coordinate of the horizontal section profile.

When optimizing the streamlined head, the bottom longitudinal section profile is set to a parabolic equation, so the value of A_{21} is 2. Without considering the deformation of the horizontal section profile near P8, the value of A_{22} is set to 1 as a constant value. The deformation of the bottom horizontal profile has little effect on train aerodynamic performance, and the values of A_{31} and A_{32} are set to 0.4 and 1 respectively to reduce the number of design variables. Usually, the maximum cross-sectional shape of the train is fixed, therefore the maximum cross-sectional shape is constant in this paper, and the values of A_{41} and A_{42} are 4 and 1, respectively. The surfaces of the nose are a gradual transition from one dot to the maximum cross-sectional shape, so the value of A_{R1} of the initial dot is given as 2. Without considering the deformation of the y-axis direction and the vicinity of the point P4 for the cab window, the corresponding parameters A_{62} and A_{63} are both given as 2 and the coordinate values of all control points are fixed values. The remaining six undetermined parameters A_{11}, A_{12}, A_{21}, P_u, g_h and A_{61} are regarded as design parameters (for their ranges, see Table 2).

The geometry controlled by the design parameters above is shown in Figure 7. It can be seen that completely different types of streamlining can be obtained by adjusting the design parameters.

4.2. CFD algorithms

In order to more accurately simulate the flow field around the train, the geometry of the train designed in this paper is given in accordance with the real geometry of the high-speed train, as shown in Figure 8. The length of the leading car and trailing car is 26.5 m, and the shape of the trailing car is the same as that of the leading car. The length L of the streamlined head is 12 m, the height is 3 m, the width is 3.2 m and the cross-sectional area is 9.3 m². The initial shape of the train is determined by the average value of the maximum value and the minimum value of each dimension in the design space. Since the last bogie of the trailing car has a great effect on aerodynamic lift, it is retained.

In this paper, the speed of the high-speed train is 300 km/h, so the Mach number is 0.245. Under this condition,
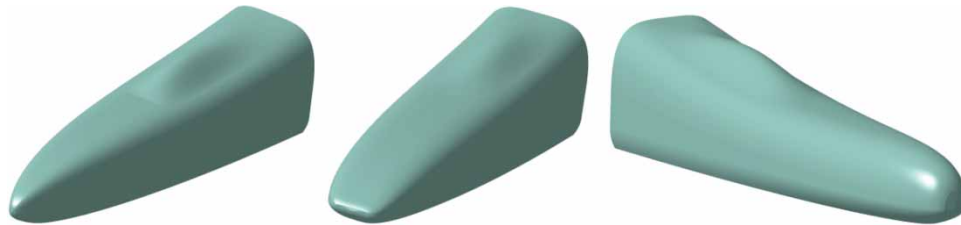

Figure 7. Different streamlines obtained by adjusting the design variables.
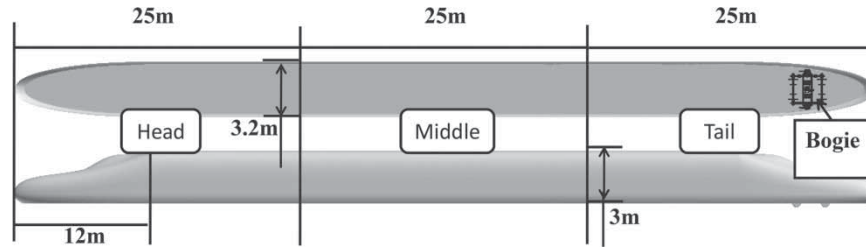
Figure 8.   Original model of the high-speed train.

the air compression characteristic has an obvious effect on the aerodynamic drag of the train. Therefore, the steady compressible Reynolds-averaged Navier-Stokes equations based on the finite volume method are used to predict the aerodynamic drag. Roe's FDS scheme is used to calculate convective fluxes, and the Lower-Upper Symmetric Gauss-Seidel (LU-SGS) is chosen for temporal discretization. The k-ω SST model is selected as the turbulence model. The standard wall functions are used near the wall so that the accuracy of the CFD results can be ensured with a limited amount of mesh.

In terms of the computational domains and boundary conditions, taking the length of the simplified train as the characteristic length L, the length of inflow direction is 1L, the length of outflow direction is 2L, the width is 1L, and the far-field height is 0.5L (see Figure 9). The flow velocity is 83.33 m/s; the far-field pressure is 1 atm, the temperature is 288 K and the reference area is the maximum cross-sectional area of the train. As a result of the compressibility calculation model, one-dimensional inviscid flow of the Riemann invariants are introduced as the far-field boundary conditions, which are also known as non-reflective boundary conditions. Inflow, outflow and the top boundaries are all set as far-field boundary conditions and the

train body is set with the non-slip solid wall boundary condition. The ground is treated as the moving wall so as to simulate the ground effect, and the moving speed is equal to the train speed.

4.3.   Mesh independence validation

Mesh quality has a direct impact on the accuracy and stability of the calculation results. Thus, grid-independent validation is firstly performed in the present paper with different amounts of spatial mesh that combine prism mesh near the wall and hexahedral mesh so as to assess the influence of different spatial mesh on the calculation results. With the thickness of the first prism layer meeting the requirement of the wall function ($30 \leq y^+ \leq 50$) that is valid to simulation the flow around high-speed trains (Yao, Guo, et al., 2012; Yao, Guo, & Yang, 2012), three sets of mesh are obtained in this paper by changing the number of grid layers in the boundary layer, increasing the mesh size and region. As can be seen in Figure 10, the value of y^+ of the body surface is mainly in the range from 30 to 50. Flowing through a stagnation point at the nose shape, the air velocity increases quickly, thus the value of is higher y^+ near the nose. Due to the development of the boundary
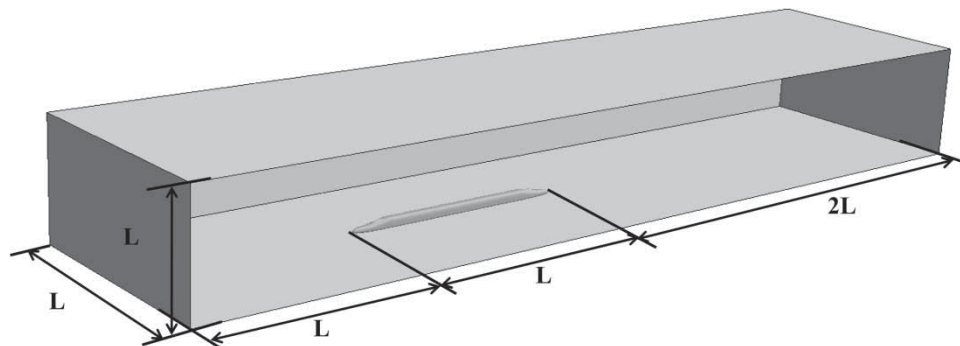

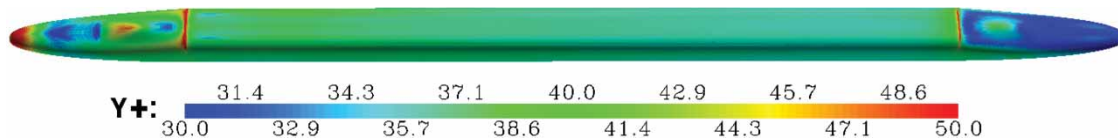Figure 9.   Computational domain.

Figure 10.   Values of y^+ around the surface of the train.

Table 3. Mesh configuration strategy and computational results.

Mesh number (millions)	First layer thickness (mm)	Prism layer number	Minimum size (mm)	Stretching ratio	Total Cd	Tail Cl
8	0.45	6	12	1.5	0.1686	0.0207
10.02	0.45	10	12	1.5	0.1672	0.0198
36.16	0.45	6	8	1.5	0.1684	0.0201

layer, the rear cone is basically in the thick boundary layer and the air flows slowly, thus the value y^+ near the rear cone is lower.

Table 3 shows the layout strategy and calculation results of the three sets of grids. As can be seen, the difference in the calculation results of the three sets of grids is not significant. Taking the result of the grids with the minimum mesh amount as the basis, the maximum difference of the aerodynamic drag of the train is 0.83%. Due to the complexity of the wake flow field (Baker, 2001), the aerodynamic lift of the trailing car is more sensitive to the grid layout strategy and the biggest difference is 4.35% for the calculation results of the three sets of grids. This basically meets the engineering accuracy requirements. Therefore, all flow field calculations in this paper are performed with the minimum-grid strategy to reduce computational time.

4.4. *Kriging surrogate model*

The Latin hypercube sampling method can be used to ensure that the sampling points represent the whole part of the design space without taking the dimension of the problem into consideration. However, this method suffers from the problem of randomness. In order to avoid this problem, the central Latin hypercube sampling method with minimum and maximum criteria based on the iterative local search algorithm has been utilized. A total of 21 initial sampling points have been chosen for training the Kriging model, of which the first 20 points are chosen as training points while the last point is chosen as the test sampling point. For the distribution of the objective function of sampling points, the maximum and minimum values of the first target (aerodynamic drag of the train) are 0.1822 and 0.1658 respectively, and the maximum minimum values of the second target (aerodynamic lift of the trail car) are 0.0340 and 0.0072 respectively. The variation range of the aerodynamic lift of the trailing car is greater, and thus the requirement for the prediction accuracy of the Kriging model for the aerodynamic lift of the trailing car is higher. Therefore, for the prediction accuracy in this paper, the prediction error of the aerodynamic drag of the train must not be greater than 1% and the prediction error of the aerodynamic lift of the trailing car must not be greater than 5%. In order to meet the prediction accuracy of the Kriging model, the minimizing response surface method has been adopted. For the Pareto solutions obtained in each iteration, three testing points are chosen

for CFD validation. If the prediction accuracy has not been met, these points are added to the training sample set so as to further refine the Kriging model until the accuracy of the model is reached. After just one iteration, the prediction accuracy of the Kriging model reached the requirement, so only 27 CFD computations were used in the whole optimization process. The optimization results based on the Kriging model are analyzed in section 5.

4.5. *Optimization process*

The optimization process of the streamlining still takes a long time, even though the Kriging response surface model has been adopted. Any errors in the design process will affect the accuracy of the optimal results. Consequently, a reasonable optimization process is required so as to improve the optimization efficiency. Figure 11 shows the optimization process designed in the present paper, which is listed as follows:

(1) Extract the key parameters in the design of streamlining by the VMF approach, and determine the range of the parameters (construct the design space).

(2) Determine the number of initial training samples which could meet the prediction accuracy of the Kriging model by experience, sample in the design space using the central Latin hypercube sampling method with the maximum and minimum criteria and obtain the initial value of the training samples.

(3) Obtain the accurate value of the objectives using the CFD approach.

(4) Train the Kriging model using a real-coded genetic-algorithm approach and obtain the optimal correlation coefficients.

(5) Based on the Kriging model, perform the optimization using MPSO-CR and obtain the Pareto solutions.

(6) Chose several solutions as test samples and perform validation using the CFD approach. Judge whether the accuracy of the solutions meets the requirement or not.

(7) If not, the test samples from the previous step are added to the training sample set, and steps3 is repeated in order to reconstruct the Kriging model.

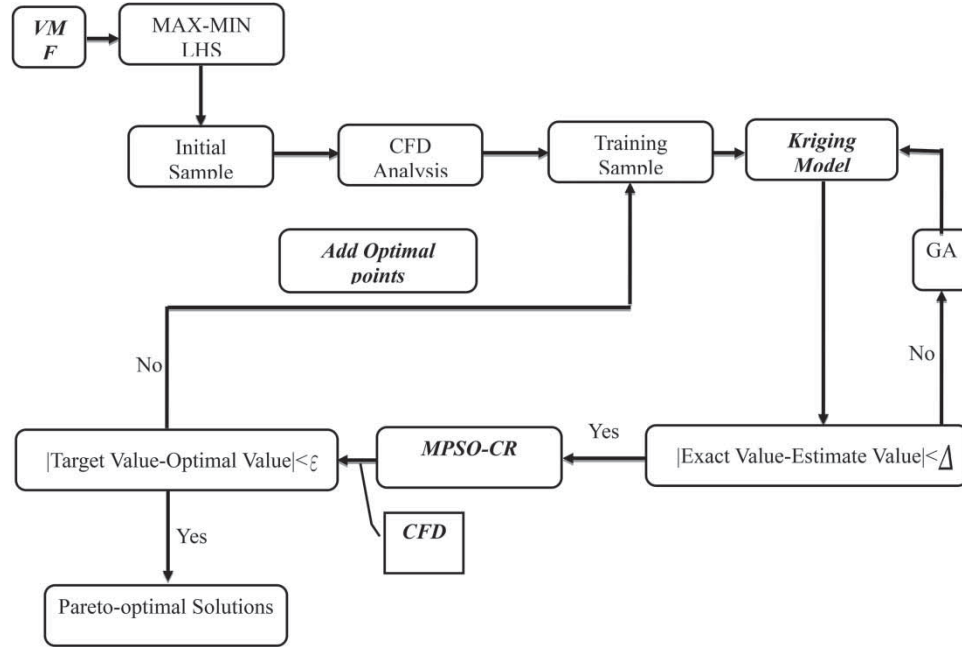(8) If the accuracy has been met then the Kriging model has been precisely constructed and the

Figure 11.   The optimization process of the streamlining of high-speed trains.

Pareto solutions obtained by the Kriging model are the final optimal solutions.

5.   Optimization results and analysis

Based on the constructed Kriging surrogate model, the Pareto optimal solution of the aerodynamic drag of the train and the aerodynamic lift of the trailing car is found using MPSO-CR. The related parameter setting of MPSO-CR is the same as the setting of test function optimization. Figure 12 shows the distribution of the Pareto-optimal solution. It can be seen that the distribution of the optimal solution is uniform, indicating that MPSO-CR has better capability of searching for optimization in complex engineering problems. Within the design space, the aerodynamic drag of the train only 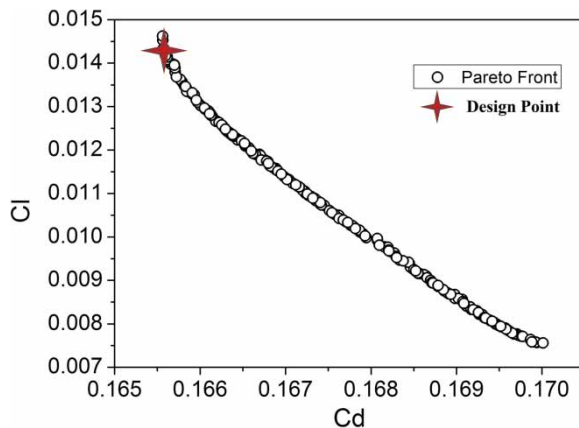receives small changes, but the aerodynamic lift of the trailing car receives big changes. In order to get a design point at which the aerodynamic drag of the train is less, the point in Figure 12 is chosen as the optimal design point.

Table 4.   Aerodynamic forces before and after optimization and the prediction accuracy of Kriging model.

Model type	Total Cd	Tail Cl
Original shape	0.1686	0.0207
Optimal shape	0.1659	0.0146
Reduction	**1.60%**	**29.47%**
Kriging model	0.1656	0.0143
Error	**0.18%**	**2.05%**

Ku et al. (2010) adopted the VMF method and Kriging model to reduce the micro-pressure wave and aerodynamic drag of a high-speed train. After optimization, the aerodynamic drag was reduced by 5.6%. Compared to a simplified CRH380A model, the aerodynamic drag of the optimization shape is reduced by 3.2% in Yao, Guo, et al. (2012). The aerodynamic drag of the optimal head of a CRH3 high-speed train was reduced by 1.85% in Sun et al. (2010), while the results of Vytla et al. (2010) showed a reduction in the aerodynamic noise of the optimal shape of 6% but an increase in aerodynamic drag of 2%. The results indicate that the aerodynamic drag of the high-speed train is not very sensitive to the design parameters if the nose length is constant. Table 4 shows the train aerodynamic forces before and after optimization and the prediction accuracy of Kriging model. As can be seen, after optimization, the aerodynamic drag of the train is reduced by 1.6%, and the aerodynamic lift of the trailing car is

Figure 12.   Pareto-optimal solution set.

Table 5. Design parameter values before and after optimization.

	A_{11}	A_{12}	A_{21}	P_u	g_h	A_{61}
Original shape	0.45	3.5	0.35	1.0	0.4	0.8
Optimal shape	0.4176	3.5942	0.4592	1.2824	0.3884	0.8959

reduced by 29.47%. The Kriging model prediction errors of the two objectives are 0.18% and 2.05% respectively; thus, the accuracy requirements of the engineering design are reached. The constructed Kriging model can map a nonlinear relationship between the design variables and optimization objectives.

Table 5 shows the design parameter values before and after optimization. The values of the design parameters of the original shape are the average of the maximum and minimum values of each parameter. After optimization, A_{11} and A_{21}, which control the bluntness and width of the nose shape, receive larger changes, and the other four

parameters receive small changes, revealing that the aerodynamic performance of the original shape is better compared with the other design points within the design space. Correction of the original shape design can be made to obtain a train shape with better aerodynamic performance.

Figure 13 shows the pressure coefficient distribution along longitudinal section profiles of the leading car and the trailing car before and after optimization. As can be seen, after optimization, the bluntness of the nose increases slightly and the incline of the windshield of the cab increases. The high-pressure area on the nose of the leading car moves to the tip of the nose, and the low-pressure area on this region moves backward due to the deformation of the windshield of the cab. There is a high pressure area in the transition area between the windshield and the cab. Low pressure near the nose and tailing cone slightly decreases, and pressure distribution moves towards zero. Therefore the upward pull of the upper part of the trailing cone is reduced, and the lift of the trailing car decreases. Pressure fluctuation at the bottom of the trailing cone is
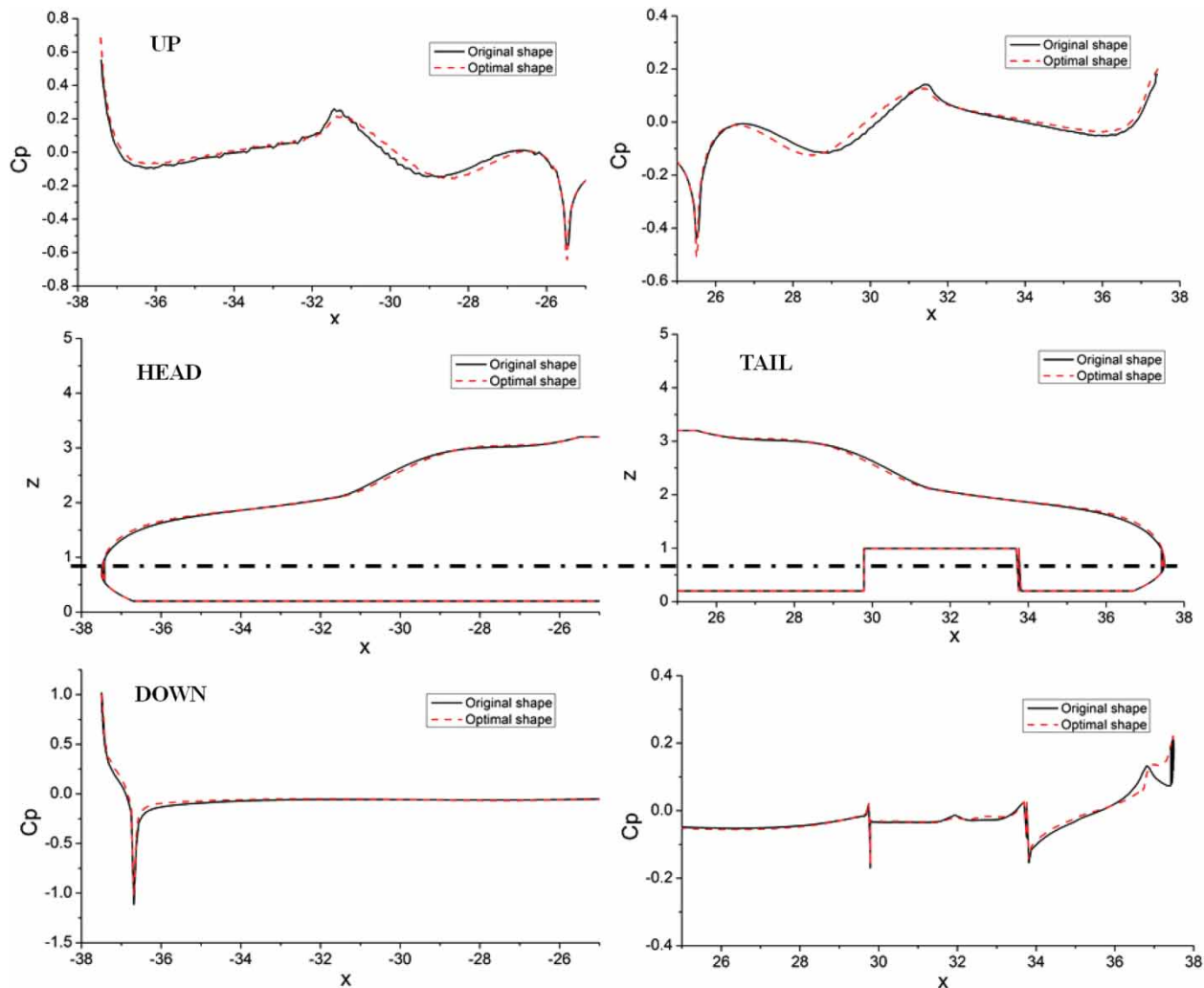

Figure 13. Pressure-coefficient distribution along longitudinal section profiles of the leading car and the trailing car before and after optimization.
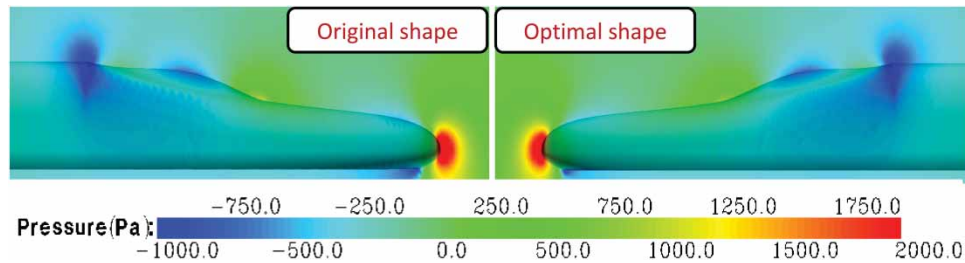
Figure 14. Pressure distribution around the leading car before and after optimization.

large, and there are two larger low pressure zones at both ends of the bogie shield.

Figure 14 shows the pressure distribution around the leading car before and after optimization. As can be seen, there is a larger high-pressure zone in the nose region, and there is a sub-high-pressure area in the transition area between the cab window and the nose. An obvious low pressure zone exists at the bottom of the nose, and a larger low pressure exists in the transition area between the nose shape and the train body. After optimization, an increase in the incline of the cab window results in faster airflow acceleration at the juncture of this area and the transition area, and then low pressure at the juncture is slightly increased. These two factors lead to reduced pressure drag of the head car to some extent.

6. Conclusion

Multi-objective PSO algorithms have been applied to many practical engineering problems. In order to improve the searching capabilities of the algorithm and obtain more satisfying optimization solutions, based on the concept of niche count and crowding distance, an MPSO was introduced. Under four test conditions, the niche count and crowding distance were used to determine the global best particle in an external file. Then a comparative analysis was carried out between the MPSO and a non-dominated sorting multi-objective adaptive genetic algorithms, real-coded and binary-coded. The results show that MPSO based on the crowding distance is best at getting the Pareto front, especially for problems with a high-dimensional and non-continuous Pareto front.

In order to verify the efficiency of MPSO to solve engineering problems, the multi-objective optimization design of the aerodynamic nose shape of high-speed trains was undertaken using a modified vehicle modeling function (MVMF) parametric method. Extracting six design parameters and taking the aerodynamic drag of the whole train (Cd) and aerodynamic lift of the trailing car (Cl) as the optimization goals, a Kriging surrogate model was constructed by using the Latin hypercube sampling method to collect 21 samples. The MPSO based on crowding distance was used for the multi-objective aerodynamic shape optimization design to find the Pareto optimization solution in the design space. The optimization results show that the

MVMF parametric method can be applied to the optimal design of the nose shape of high-speed trains. Because of less design parameters of actual control, this method can effectively shorten the optimization cycle and improve optimization efficiency for engineering optimization problems that need a large amount of computation, and can result in a new, more streamlined head for high-speed trains.

After optimization, compared to the original shape, the Cd and Cl of the optimal shape were reduced by 1.6% and 29.74%, respectively. The obvious improvement of the train aerodynamic performance shows that the optimization algorithm in this paper can be applied to practical engineering problems.

Disclosure statement

No potential conflict of interest was reported by the authors.

References

Arakawa, M., & Hagiwara, I. (1998). Development of adaptive real range genetic algorithms. *JSME International Journal, Series C*, *41*(4), 969–977.

Baker, C. J. (2001). Flow and dispersion in ground vehicle wakes. *Journal of Fluids and Structures*, *15*, 1031–1060.

Coello, C. A. C., Pulido, G. T., & Lechuga, M. S. (2004). Handling multiple objectives with particle swarm optimization. *IEEE Transactions on Evolutionary Computation*, *8*(3), 256–279.

Deb, K., Mohan, M., & Mishra, S. (2005). Evaluating the ϵ-domination based multi-objective evolutionary algorithm for a quick computation of Pareto-optimal solutions. *Evolutionary Computation*, *13*, 501–525.

Dehuri, S., Roy, R., Cho, S. B., & Ghosh, A. (2012). An improved swarm optimized functional link artificial neural network(ISO-FLANN) for classification. *The Journal of Systems and Software*, *85*, 1333–1345.

Fonseca, C. M., & Fleming, P. J. (1994). *An overview of evolutionary algorithms in multi-objective optimization[P]*. (Technical report). Sheffield, UK: Department of Automatic Control and Systems Engineering, University of Sheffield.

Hu, X., & Eberhart, R. (2002). *Multiobjective optimization using dynamic neighborhood particle swarm optimization*. Proceedings of the 2002 Congress on Evolutionary Computation.

Kennedy, J., & Eberhart, R. C. (1995). *Particle swarm optimization*. Proceeding of the 1995 IEEE International Conference on Neural Network. Perth, Australia, 1942–1948.

Kulfan, B. M., & Bussoletti, J. E. (2006). *Fundamental parametric geometry representations for aircraft component shapes*. 11th AIAA/ISSMO Multidisciplinary Analysis and Optimization Conference, Portsmouth, VA: 1–42.

Ku, Y. C., Kwak, M. H., Park, H. I., et al. (2010). *Multiobjective optimization of high-speed train nose shape using the vehicle modeling function*. 48th AIAA aerospace sciences meeting, Orlando, USA.

Kwon, H. B., Jang, K. H., Kim, Y. S., et al. (2001). Nose shape optimization of high-speed train for minimization of tunnel sonic boom. *Japan Society Mechanical Engineering*, *4*, 890–899.

Lee, J., & Kim, J. H. (2008). Approximate optimization of high-speed train nose shape for reducing micropressure wave. *Industrial Applications*, *35*, 79–87.

Li, X. (2003). *A non-dominated sorting particle swarm optimizer for multiobjective optimization*. Proceeding of Genetic and Evolutionary Computation GECCO 2003: Genetic and Evolutionary Computation Conference, Springer. 2003: 37–48.

Moore, J., & Chapman, R. (1999). Application of particle swarm to multi-objective optimization. Auburn, Alabama: Department of Computer Science and Software Engineering, Auburn University.

Parsopoulos, K. E., & Vrahatis, M. N. (2002). Particle swarm optimization method in multiobjective problems. In *Proceedings of the 2002 ACM symposium on Applied computing*, ACM Press New York NY, USA, 2002: 603–607.

Pratab, A., & Deb, K. (2000). A Fast elitist non-dominated Sorting Genetic Algorithm for Multi-objective Optimization: NSGA-II. (Kan-GAL report 200001). Kanpur, India: Indian institute of technology.

Rho, J. H., Ku, Y. C., Kee, J. D., et al. (2009). Development of vehicle modeling function for 3-dimensional shape optimization. *Journal of Mechanical Design*, *131*(12), 121004.

Schott, J. R. (1995). Fault tolerant design using single and multicriteria genetic algorithm optimization.

Srinivas, N., & Deb, K. (1994). Multi-objective optimization using nondominated sorting in genetic algorithms. *Evolutionary Computation*, *2*(3), 221–248.

Sun, Z. X., Song, J. J., & An, Y. R. (2010). Optimization of the nose shape of the CRH3 high speed train. *Science China Technological Sciences*, *53*, 3356–3364.

Vytla, V. V., Huang, P. G., & Penmetsa, R. C. (2010). Multi objective aerodynamic shape optimization of high speed train nose using adaptive surrogate model. *AIAA-2010–4383*.

Yang, G. W., Chen, D. W., & Cui, K. (2009). Response surface technique for static aeroelastic optimization on a high-aspect-ratio wing. *Journal of Aircraft*, *46*(4), 1444–1450.

Yao, S. B., Guo, D. L., Sun, Z. X., et al. (2012). Multi-objective optimization of the streamlined head of high-speed trains based on the Kriging model. *Science China Technological Sciences*, *55*(12), 3494–3508.

Yao, S. B., Guo, D. L., & Yang, G. W. (2012). Three-dimensional optimization design of high-speed train nose based on GA-GRNN. *Science China Technological Sciences*, *55*(11), 3118–3130.